

Contents lists available at ScienceDirect

CIRP Journal of Manufacturing Science and Technology

journal homepage: www.elsevier.com/locate/cirpj





Thermo-mechanical finite element analysis of the solid-state metal deposition via lateral friction surfacing

Ebrahim Seidi ^{a,*}, Scott F. Miller ^b

- ^a Arkansas Tech University, Russellville, AR, USA
- ^b University of Hawaii at Manoa, Honolulu, HI, USA

ARTICLE INFO

Keywords:
Finite element method
Friction deposition
Metal coating
Thermo-mechanical simulation
Numerical analysis

ABSTRACT

Lateral friction surfacing (LFS) is a novel variation of the friction surfacing (FS) process for solid-state fabrication of ultra-thin and smooth metal coatings. In the LFS technique, pressing the lateral side of a rotating rod against the substrate's surface generates frictional heat and plastic deformation, leading to the deposition of consumable material from the lateral surface of the rod onto the substrate. This study presents numerical analysis for such a complex coupled thermo-mechanical process to investigate the distribution of various variables such as temperatures, local pressure, stress, and strain throughout the consumable rod and substrate. A finite element model of the process was developed through ABAQUS/Explicit method to investigate the thermo-mechanical response of rod and substrate materials by incorporating various features such as process parameters, mechanical behaviors of materials, temperature-dependent material properties, and failure criteria. The finite element model was validated by conducting experimental analysis using the same materials and values of process parameters. The finite element simulation results were consistent with previous experiments and affirmed that process temperature is lower than in conventional FS and localized in a small area, which can reduce thermal impacts on the consumable rod and substrate materials. Although the majority of the frictional heat was transferred to the Al6061-T6 rod due to its higher thermal conductivity, it was revealed that the maximum process temperature occurred on the mild steel substrate. The results of the study demonstrate that selecting an appropriate dwellphase duration not only enhances the material's temperature to facilitate improved deposition but also ensures more consistent contact across all points along the rod's side, resulting in a uniform deposition.

1. Introduction

FS is an additive manufacturing technique for metal deposition from the end of a consumable rod, which has been derived from friction stir processing for surface modification [1]. This technology provides fine-grained coatings through solid-state metal deposition for a broad range of rod-substrate materials to perform localized surface engineering. There are several studies on FS as a solid-state deposition technique to remove keyholes created by friction stir processing [2–4], evaluate and improve the surface hardness [5–7], wear performance [8,9], corrosion performance [10–12], and create composite coatings [13–15].

The heat required for FS process is generated by friction at the interface of the rod and substrate and plastic deformation of the consumable material; however, the majority of generated heat energy is due to plastic deformation [16]. Liu et al. developed a finite element model to investigate the heat generation and temperature distribution in

the consumable rod used in FS process [17]. In addition, an experimental analysis was conducted to validate the finite element method (FEM) results, which exhibited that the simulation results were consistent with the experiments.

Recently, more investigations have been carried out to simulate the solid-state metal deposition through the FS approach by employing three-dimensional finite element modeling to evaluate the thermal and mechanical responses during the fabrication process. The FEM result of deposition of Al2024 onto Al2024 showed a slightly higher maximum process temperature for the advancing side compared to the retreating sides of the deposit [18]. Also, it was revealed that increasing the axial feed rate and the rotational speed of the consumable rod resulted in increasing the maximum process temperature and strain rate, while a higher traverse speed resulted in a higher strain rate and reduced maximum process temperature.

In another investigation, the thermo-mechanical behavior of Al2024 fabricated onto Al1050 substrate through FS process was evaluated by

^{*} Correspondence to: Assistant Professor of Mechanical Engineering, Arkansas Tech University. E-mail address: eseidi@atu.edu (E. Seidi).

| Nomenci | lature | h | heat convection coefficient |
|---------------------|--|--------------------------|--|
| ρ | material density | σ | Stefan-Boltzman constant |
| С | specific heat capacity | \boldsymbol{A} | quasi-static yield strength |
| t | time | В | hardening modulus |
| T | temperature | C | strain rate sensitivity coefficient |
| k | thermal conductivity | $arepsilon^{pl}$ | effective plastic strain |
| G | heat generation rate | n | work-hardening index |
| x, y, z | spatial coordinates | m | thermal softening index |
| \dot{q}_f | frictional heat generation rate | $\dot{arepsilon}_0$ | reference plastic strain rate |
| r | consumable rod radius | $\dot{\varepsilon}^{pl}$ | effective plastic strain rate |
| ω | angular velocity of the rotating rod | T_{melt} | melting point temperature |
| μ | coefficient of friction | $T_{transition}$ | transition temperature |
| F_n | normal force | T_{room} | room temperature |
| \dot{q}_{pl} | plastic deformation heat generation rate | $arepsilon^f$ | strain at fracture |
| η | inelastic heat fraction | D_i | material dependent parameters ($i = 1, 2,, 5$) |
| $\overline{\sigma}$ | equivalent stress | σ^* | stress triaxiality |
| ÷pl € | equivalent plastic strain rate | p | hydrostatic pressure |
| R_{rod} | ratio of heat partition into the rod | $\overline{\sigma}_{ u}$ | von Mises equivalent stress |
| k_{rod} | rod thermal conductivity | $arDeltaarepsilon^p$ | increment in the equivalent plastic strain |
| $k_{substrate}$ | substrate thermal conductivity | $arepsilon^f$ | equivalent fracture strain at the present condition of |
| q_{conv} | heat dissipated through convection | | temperature |
| q_{rad} | heat dissipated through radiation | D_f | damage variable |

establishing a finite element model using ABAQUS software [16]. The simulation results revealed that the plastic strain on the advancing side of the deposit was higher than that on the retreating side. Nevertheless, the highest level of strain in the coating was significantly less than that at the tip of the consumable rod. Deposition of the Al5083 consumable material onto an Al5052 substrate was investigated by developing an ABAQUS finite element model [19]. Due to the high thermal conductivity of aluminum, no significant difference in the maximum process temperature of the advancing and retreating sides was observed. Also, a cold substrate simply results in a rapid cooling process at the interface of the coating/substrate, reducing the deposit temperature to the substrate temperature in a few seconds. This phenomenon resulted in the formation of finer grain structures at the interface compared to the upper side of the deposit.

A recently developed technique called LFS approach is a novel variation of the FS process for solid-state extremely-thin and smooth metal coating fabrication [20]. In this new lateral configuration, material is transferred from the radial surface of the rotary consumable rod as the side of the rod rubs across the substrate surface, as shown in Fig. 1. To evaluate the potential of this novel approach for developing thin

coating layers, different aluminum alloys, such as Al2011, Al6061, and Al7075, were surfaced onto 1018 carbon steel substrate with a particular focus on the influence of process factors on the deposits [21]. The experimental results revealed that the deposit quality relies on the materials and process factors such as rod rotational speed and normal force which can define the input energy into the process. Moreover, it was exhibited that material properties such as melting point and thermal conductivity may create limitations in using some range of process parameters values to avoid material breakdown due to severe plastic deformation.

Further investigations on material characteristics [22] and corrosion performance [23] of deposits fabricated by LFS were conducted. Furthermore, this technique was examined by performing multilayer friction deposition of Al6063 onto A36 mild carbon steel [24] and Al6061 onto AISI 1018 and AISI 4140 [25] to assess the potential of this approach for additive manufacturing purposes. Experimental analyses exhibited that the reverse material transfer from the deposited coating to the radial surface of the consumable rod limits the thickness of the fabricated coating in multilayer deposition.

The experimental analyses of the LFS process exhibited the complex

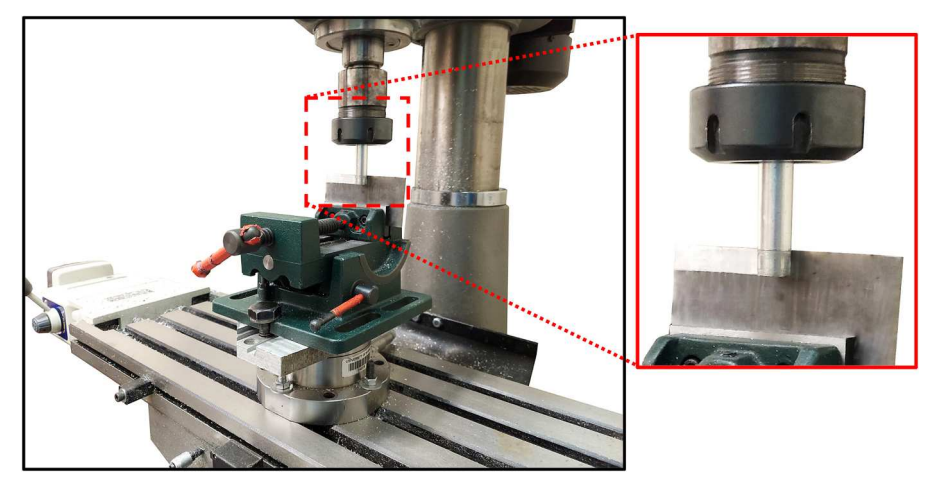


Fig. 1. Ultra-thin coating fabrication through LFS process.

relationship between process parameters and the quality of fabricated deposits. Despite the experimental investigations, the LFS process has not been studied numerically. The current study is focused on finite element modeling of the LFS process and is a key research to understand heat generation, stress, strain, and temperature distribution throughout the consumable rod and substrate to investigate the thermo-mechanical responses of material in this novel metal deposition approach [26]. The Abaqus/Explicit approach uses small intervals to achieve an accurate numerical solution, which makes it an appropriate formulation for solving high-speed dynamic and complex problems [27].

FEM of FS has been reviewed, however, the difference in the LFS process is that the radial surface of the consumable tool is in contact with the surface of the substrate instead of the end of the consumable tool. which results in constant relative velocity in the area of contact (i.e., no change in radius or retreating and advancing side) and lower process temperature in the experiments. Therefore, the different distributions of stress, strain, and temperature need to be quantified. By utilizing advanced finite element analysis, this study offers insights into temperature, stress, and strain distributions throughout the rod and substrate during the LFS process. This enhances comprehension of the complex process, highlighting its capability for thin, smooth, and consistent metal coating deposition at significantly lower process temperatures compared to the traditional approach. In the coupled thermomechanical analysis, the stress analysis results depend on the temperature distribution, and the temperature distribution highly relies on the thermo-mechanical behavior of the materials. This study presents a coupled thermo-mechanical modeling using ABAQUS software to investigate the LFS of Al6061-T6 rod onto mild steel substrate. For this purpose, many features have been incorporated into the finite element modeling, such as process parameters, mechanical behaviors of materials, temperature-dependent material properties, failure criteria, etc. In addition, the process temperature was measured using an infrared camera. The emissivity of the surface for infrared thermography was measured using a J-type thermocouple and a furnace. Finally, the temperature at the processing zone has been taken from the model to be compared with the experimental results to validate the model.

2. Thermo-mechanical finite element modeling formulation

The three-dimensional, thermo-mechanical finite element model has been developed to simulate the LFS process and provide detailed information about temperature, stress, and strain distribution. The governing theory behind the heat transfer process can be expressed mathematically in Eq. (1):

$$\rho c \frac{\partial T}{\partial t} = k \left(\frac{\partial^2 T}{\partial x^2} + \frac{\partial^2 T}{\partial y^2} + \frac{\partial^2 T}{\partial z^2} \right) + G \tag{1}$$

where ρ is material density, c is specific heat capacity, t is time, T is temperature, k is thermal conductivity, G is the rate of heat generation, and x, y, and z are spatial coordinates. There are two crucial sources of heat generation in this process, including frictional heat and plastic deformation heat generation, as presented in Eq. (2).

$$G = \dot{q}_f + \dot{q}_{pl} \tag{2}$$

The frictional heat generation in the process is due to the contact between the rotating consumable rod and substrate, which can be presented by Coulomb's friction law, $\dot{q}_f=2\pi r\omega\mu F_n$, in which \dot{q}_f is the frictional heat generation rate, r is consumable rod radius, ω is angular velocity of the rotating rod, μ is coefficient of friction between surfaces, and F_n is the normal force. The irreversible plastic deformation of materials results in a heat generation rate that can be expressed by $\dot{q}_{pl}=\eta \overline{\sigma} \dot{\varepsilon}^{pl}$, in which $\dot{\overline{\varepsilon}}^{pl}$ is equivalent plastic strain rate, $\overline{\sigma}$ is equivalent stress, and η is inelastic heat fraction which is set to 0.9 [28].

The ABAQUS/Explicit method employed in this study uses a central

difference rule and explicitly incorporates the governing equations of the system with respect to time. In the explicit technique, the state of the system (stresses, strains, temperatures, accelerations, velocities, displacements, etc.) at the end of each time increment is calculated based on the state of the system at the beginning of the increment. The element deletion technique was employed in the model, in which a material point will be deactivated once it reaches a value above its load-carrying capacity [29].

2.1. Process parameters, material properties, and mesh

substrate mild with the dimension steel of $100~\text{mm} \times 60~\text{mm} \times 7~\text{mm}$ and a consumable rod made of aluminum with a length of 100 mm and a diameter of 12.7 mm (0.5") were modeled in the finite element model [30]. The LFS process was modeled in three phases, dwell phase, deposition phase, and cooling phase. The total time 5 s, 6 s, and 2 s were set for the dwell phase, deposition phase (traverse motion), and cooling phase, respectively. The time values have been deliberately selected to be minimal to ensure that every stage of the process can be evaluated efficiently within a short coating pass, thereby decreasing the computational time. The rod rotational speed was set to 2300 rpm or 240.85 rad/s, and a linearly increasing normal force with a maximum of 150 N was gradually applied on the rod during the first 2.5 s of the dwell phase, as shown in Fig. 2. Then, the constant normal force of 150 N was applied on the lateral surface of the consumable rod for the rest of the dwell phase and the entire deposition phase. During the dwell and deposition phase, the only restriction on substrate movement in the direction perpendicular to its transverse motion is the presence of the consumable rod, which limits the substrate's movement upon contact and generates the contact force and frictional heat required for the deposition process. Moreover, the constant traverse speed of the substrate was set to 44 mm/min during the deposition phase. The values of process parameters have been chosen based on prior experimental experiences concerning determining the optimal process parameters for creating a high-quality coating layer.

To accurately represent the heat exchange between the processing zone and its surrounding environment in the model, the dissipation of heat via conduction, convection, and radiation has been taken into account during the modeling process. The temperature–dependence friction coefficients are presented in Table 1, and it was assumed that the entire dissipated energy caused by friction at the rod/substrate interface was converted to heat. The generated heat at the processing zone was assumed to be divided between rod and substrate based on their ratio of thermal conductivity [28]. The ratio of heat partition into the rod, R_{rod} , can be calculated by Eq. (3):

$$R_{rod} = \frac{k_{rod}}{k_{rod} + k_{substrate}} \tag{3}$$

where k_{rod} and $k_{substrate}$ are the thermal conductivity of the consumable rod and substrate, respectively. As shown in Tables 2 and 3, the thermal conductivity of Al6061-T6 consumable rod and steel substrate at room temperature are 167 and 34.5 W/(m.K), respectively. The ratio of frictional heat generated at the processing zone transferred to the aluminum rod is $R_{rod}=0.8288$, indicating that most of the heat generated was transferred to the aluminum rod.

As shown in Fig. 3, half of the steel substrate was clamped in a vise made of steel, and a coarse mesh was employed for that part of the steel substrate due to its lower importance and impact on the process. Those parts of the substrate surface in contact with vise jaws were mechanically tied with the vise to consider the effects of the vise on the process. The top half of the steel substrate surface and part of the rod out of the tool holder were under free convection. The ambient air temperature was 20 °C, and the convection coefficient of steel substrate [31] and aluminum [28] rod were set to 25 W/m^2K and 30 W/m^2K , respectively.

Moreover, the radiation from the surfaces to the surrounding area

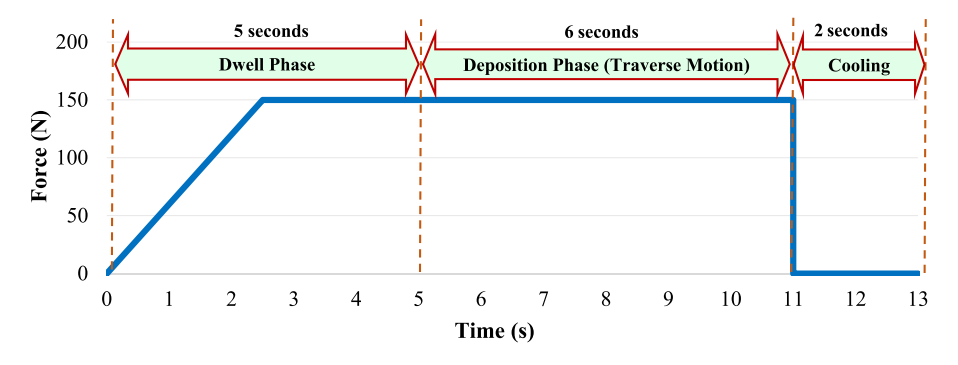


Fig. 2. The applied normal force between the consumable rod and substrate in the simulation.

Table 1
Friction coefficient as function of temperature [32].

| Temperature [K] | 295.15 | 307.85 | 366.15 | 420.65 | 483.75 | 533.15 | 588.75 | 644.25 | 699.85 | 952 |
|----------------------|--------|--------|--------|--------|--------|--------|--------|--------|--------|-----|
| Friction Coefficient | 0.61 | 0.545 | 0.259 | 0.115 | 0.064 | 0.047 | 0.035 | 0.02 | 0.007 | 0 |

 Table 2

 Temperature dependent material properties for Al6061-T6 [32].

| Temperature [K] | 310.95 | 366.45 | 422.15 | 477.15 | 533.15 | 589.15 | 644.13 | 700.15 |
|--|--------|--------|--------|--------|--------|--------|--------|--------|
| Density [Kg/m ³] | 2690 | 2690 | 2670 | 2660 | 2660 | 2630 | 2630 | 2600 |
| Heat capacity [J/Kg.K] | 945 | 978 | 1000 | 1030 | 1052 | 1080 | 1100 | 1130 |
| Thermal Conductivity [W/m.K] | 167 | 177 | 184 | 192 | 201 | 207 | 217 | 223 |
| Thermal Expansion [1/K]×10 ⁻⁶ | 23.5 | 24.6 | 25.7 | 26.6 | 27.6 | 28.5 | 29.6 | 30.7 |
| Young's Modulus [GPa] | 68.5 | 66.2 | 63.1 | 59.2 | 54 | 47.5 | 40.3 | 31.7 |

Table 3Temperature dependent material properties for mild steel [32].

| P P P P | · F | | | | | | |
|--|--------|--------|--------|--------|--------|--------|--------|
| Temperature [K] | 273.15 | 371.15 | 474.15 | 589.15 | 701.15 | 844.15 | 923.15 |
| Heat capacity [J/Kg.K] | 470 | 485 | 520 | 560 | 620 | 700 | 760 |
| Thermal Conductivity [W/m.K] | 34.5 | 34.5 | 33.8 | 31 | 28.5 | 26.5 | 25.8 |
| Thermal Expansion [1/K]×10 ⁻⁶ | 1.17 | | | | | | |
| Young's Modulus [GPa] | 207 | | | | | | |
| Density [Kg/m ³] | 7800 | | | | | | |

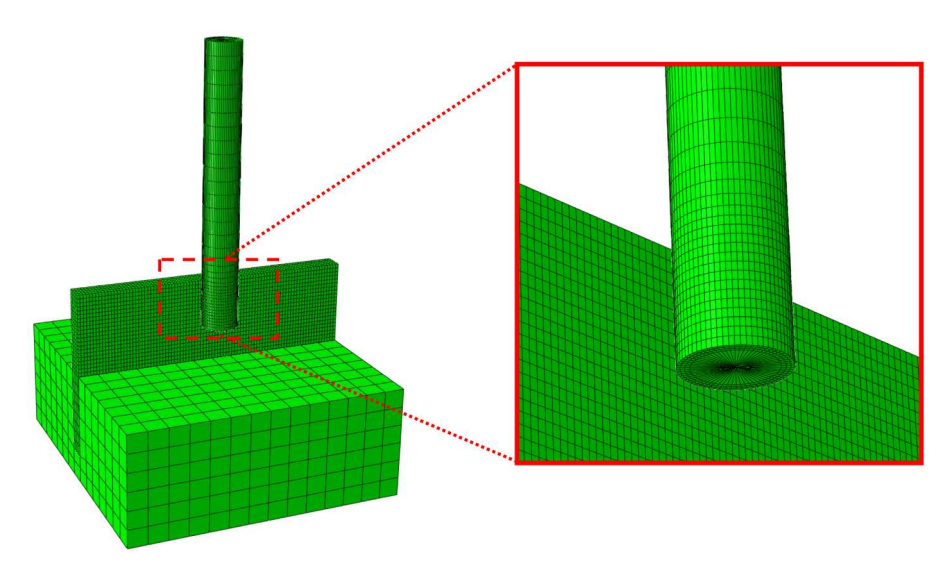


Fig. 3. Beginning mesh of rod, substrate, and vice in FEM simulation.

was considered by the Stefan-Boltzmann relation [31]. The heat convection and conduction formulas can be presented by Eqs. (4) and (5):

$$q_{conv} = -h(T - T_0) \tag{4}$$

$$q_{rad} = -\varepsilon \sigma (T^4 - T_0^4) \tag{5}$$

where q_{conv} and q_{rad} are heat dissipated from surfaces through convection and radiation, h is the heat convection coefficient of the surface (W/m^2K) , ε is the emissivity, and σ is the Stefan-Boltzman constant $(5.67 \times 10^{-8} \, W/m^2K^4)$.

The mesh characteristics of the 3D model are presented in Table 4. The rod and substrate were modeled with three-dimensional continuum elements of wedges (C3D6) and brick (C3D8T), respectively. The element size is one of the critical parameters in FEM. Employing a coarse mesh in the model results in severe distortion of many elements, which leads to the deletion of those elements, while excessive mesh refinement dramatically increases the computational time. Moreover, the LFS process requires a longer processing time compared to many other mechanical phenomena, such as impact that happens in a fraction of a second. Therefore, the LFS model should analyze the process in at least a few seconds to demonstrate the behavior of materials during this process. These limitations emphasize the importance of the element mesh size, which should be optimized to offer a good balance between computational cost and the accuracy of the results.

The material model adopted for the steel substrate was the isotropic linear elastic model, incorporating uniform density and isotropic temperature-dependent conductivity. This model is appropriate for simulating the mechanical behavior and heat transfer characteristics of the steel substrate in this study, as it was assumed that the steel substrate does not experience failure in the deposition of the aluminum coating. In order to characterize the thermal softening and plastic deformation of the Al6061-T6 consumable rod during the LFS process, the Johnson-Cook material model has been employed in the finite element model.

2.2. 2.2 Johnson-cook material model

Material structural models incorporate mathematical criteria to define the relationships between flow stress as a function of temperature, strain, strain rate, and strain hardening [33]. Therefore, the Johnson-Cook model was employed, which is capable of considering high strain rates and temperature changes that result in thermal softening and large plastic deformation. This model is presented by Eq. (6), and the Johnson-Cook parameters for Al6061-T6 are presented in Table 5

$$\sigma = [A + B(\varepsilon^{pl})^n][1 + C\ln(\dot{\varepsilon}^{pl}/\dot{\varepsilon}_0)][1 - \widehat{T}^m]$$
(6)

$$\hat{T} = \left\{ \begin{array}{l} 0: T < T_{\textit{transition}} \\ (T - T_{\textit{transition}}) / (T_{\textit{melt}} - T_{\textit{transition}}): \quad T_{\textit{transition}} \leq T \leq T_{\textit{melt}} \\ 1: T > T_{\textit{melt}} \end{array} \right\}$$

where σ is the equivalent stress, A is the quasi-static yield strength of the material (MPa), B is the hardening modulus (MPa), C is the strain rate sensitivity coefficient, ε^{pl} is the effective plastic strain, n is the work-hardening index, and m is the thermal softening index [34]. Moreover, $\dot{\varepsilon}^{pl}/\dot{\varepsilon}_0$ is the equivalent plastic strain rate for the reference plastic strain rate of $\dot{\varepsilon}_0 = 1.0 \text{s}^{-1}$ and $\dot{\varepsilon}^{pl}$ is the effective plastic strain rate. This equation consists of three different terms, and the effects of

Table 4Mesh characteristics of the 3D model.

| | Nodes | Elements | Element Type |
|-----------|-------|----------|--------------|
| Rod | 4834 | 6912 | C3D6T |
| Substrate | 13650 | 10440 | C3D8T |

elasto-plastic, viscosity, and thermal softening are presented by the first, second, and third sets of brackets, respectively. T_{melt} and $T_{transition}$ represent the melting point temperature and transition temperature, respectively. The room temperature 293.15 K (20 °C) is typically selected as the transition temperature. It should be noted that all the temperatures are in Kelvin. In the case that $T \geq T_{melt}$, the material is liquified and it behaves as a fluid, thus, the shear resistance is zero, and therefore, $\sigma=0$

The Johnson-Cook damage model incorporates the influence of a wide range of parameters on the yield strain of the material [33]. Compared to other damage criteria, the Johnson-Cook damage model presented in [36] better expresses local softening behaviors using temperature-dependent parameters, strain rate, and pressure [37]. Based on the Johnson-Cook damage criterion, the strain at fracture can be presented by Eq. (7):

$$\varepsilon^{f} = \left[D_{1} + D_{2} \exp(D_{3} \sigma^{*})\right] \left[1 + D_{4} \ln\left(\frac{\dot{\varepsilon}^{p}}{\dot{\varepsilon}_{0}}\right)\right] \left[1 + D_{5} \left(\frac{T - T_{room}}{T_{melt} - T_{room}}\right)\right]$$
(7)

$$\sigma^* = \frac{p}{\overline{\sigma}_v}$$

where D_i , i=1, 2,..., 5 are material dependent parameters presented in Table 6, and σ^* is called stress triaxiality, which can be calculated as the ratio of hydrostatic pressure p, divided by von Mises equivalent stress $\bar{\sigma}_v$. The first, second, and third brackets in Eq. (7) describe the effects of pressure, strain rate, and thermal softening on the strain at fracture, respectively. The damage evolution can be expressed by the damage variable D_f , as presented by Eq. (8):

$$D_f = \sum \frac{\Delta \varepsilon^p}{\varepsilon^f} \tag{8}$$

where $\Delta \varepsilon^p$ is the increment in the equivalent plastic strain and ε^f is the equivalent fracture strain at the present condition of temperature, stress, strain rate, and hydrostatic pressure. The fracture is assumed to happen when for at least one material element, D_f reaches to its maximum value $(D_f=1)$ [35].

3. Experimental analysis for validating the finite element model

3.1. Friction surfacing process

An experimental examination has been performed to evaluate the effects of process parameters, materials, and conditions on the process temperature for validating the result of finite element modeling. For this purpose, the LFS of Al6061-T6 on mild steel was conducted, and a mild steel substrate with the dimension of $100~\text{mm} \times 60~\text{mm} \times 7~\text{mm}$, and an aluminum rod with 100~mm in length and 12.7~mm in diameter were employed. During the LFS process, force measurement was performed utilizing a Kistler drilling dynamometer type 9272, LabVIEW programming, and data acquisition systems.

In order to provide a similar process condition in the experiment, the normal applied force was manually controlled thoroughly. During the first 2.5 s of the dwell phase, the normal force was gradually increased to 150 N, the value defined as the deposition force, and then kept constant during the rest of the dwell phase and the entire deposition phase. The coating fabrication occurs in the deposition phase, which lasted for a duration of 6 s at a traverse speed of 44 mm/min, resulting in a 4.4 mm deposit. The length of the contact line between the consumable rod and the substrate determines the second dimension of the coating, which was set to 15 mm. Therefore, a 15 mm \times 4.4 mm aluminum coating was fabricated in this process. At the beginning of the cooling phase, the consumable rod was removed from the substrate surface to zero out the normal force and terminate the deposition phase. The result of the real-time load measurement is presented in Fig. 4 with the moving average of three points, showing that the experimental normal load data closely

Table 5
Johnson-Cook parameters for Al6061-T6 [35].

| Parameter [unit] | A[MPa] | B[MPa] | n | m | $T_{melt}[K]$ | $T_{transition}[K]$ | С | $\dot{\varepsilon}_0[s^{-1}]$ |
|------------------|--------|--------|------|------|---------------|---------------------|-------|-------------------------------|
| Value | 324 | 114 | 0.42 | 1.34 | 952 | 293.15 | 0.002 | 1 |

Table 6Jonson-Cook damage parameters for Al6061-T6 [35].

| Parameters: | D1 | D2 | D3 | D4 | D5 |
|---------------------|-------|------|-------|----|------|
| Material: Al6061-T6 | -0.77 | 1.45 | -0.47 | 0 | 1.60 |

follows the trend of the force data employed in the finite element model.

3.2. Temperature measurement

The process temperature at the interface of the consumable rod and substrate was recorded using a thermal imaging camera type FLIR SC655. The infrared camera was located at a proper distance of 0.5 m from the processing area in a way it made an angle of 10 degrees with the surface of the substrate. In order to accurately calculate the emissivity of the substrate, a thermocouple type J and a furnace were employed. The steel substrate was placed inside a furnace to increase its temperature up to 200 $^{\circ}$ C, as shown in Fig. 5, and the substrate temperature was measured using the thermocouple and the infrared camera simultaneously, and the emissivity of the steel substrate was calculated to be in the range of 0.55 to 0.65. The average value of this range, 0.6, was employed as the substrate emissivity in the experiment and the FEM.

4. Results of experimental and finite element analyses

The mechanical and thermal responses during LFS of Al6061 consumable rod onto mild-steel substrate were evaluated through experimental analysis and FEM. In the FEM simulation, different responses of the work material, such as contact force, temperature, material point velocity, stress, and strain, were evaluated. Fig. 6 presents the unique nodal contact force applied to four different material points along the rod axis at the processing zone. The increasing trend of applied force during the first half of the dwell phase (first 2.5 s) of the process is noticeable. Although the consumable rod rotates with a high rotational speed of 2300 rpm, the contact force data clearly shows that every single point on the radial surface of the rod at the processing zone does not come into contact with the substrate at every single revolution. This phenomenon is due to the harmonic vibration caused by periodic excitations generated as a response to the dynamic system in the FEM. The maximum reaction force on the lateral side of the consumable rod can be calculated as the summation of the average values of contact forces at each point.

It should be noted that the location of the maximum contact force on the radial surface of the rod may not be precisely located on the mesh nodes; therefore, all the parameters associated with the contact force may be slightly varied if a smaller and different type of mesh is employed. Also, the finite element analysis of the LFS process takes a very long time due to the complex nature of the process and material behavior, as well as the large total number of increments, since the 13 s process can be considered a very long time for an explicit solver. Employing a finer mesh can improve the accuracy of the results; however, it significantly increases the computational time of the simulation. Mass scaling has been avoided in the simulation due to the potential of altering the mass matrix and leading to inaccurate results, which requires thorough evaluation and careful validation before it can be deemed suitable for use in any simulation. In this study, about 55 full days were required to simulate only 13 s of the process using an 11th Gen Intel (R) Core (TM) i7-11700 K @ 3.60 GHz processor, and this long processing time was a limitation in adopting finer mesh.

The FEM results show that the applied force was not supported by all the material points on the radial surface of the rod at the processing zone. Fig. 6 revealed that the rod nodes close to the top edge of the

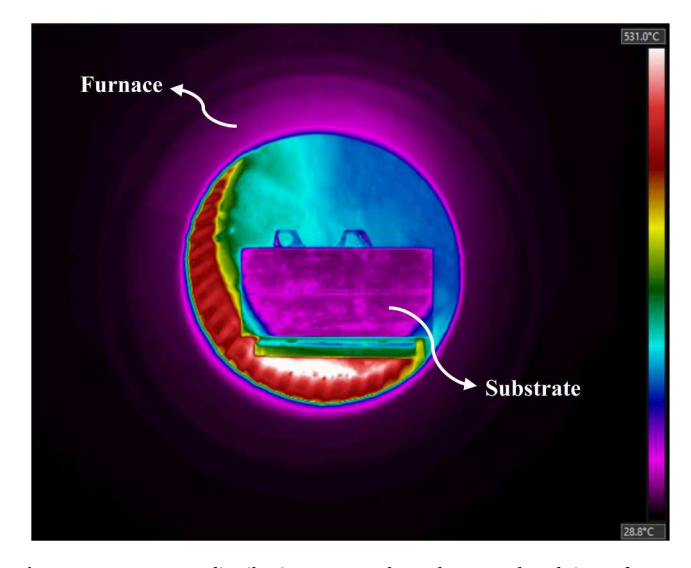


Fig. 5. Temperature distribution across the substrate placed in a furnace recorded by IR camera during measurement of steel emissivity.

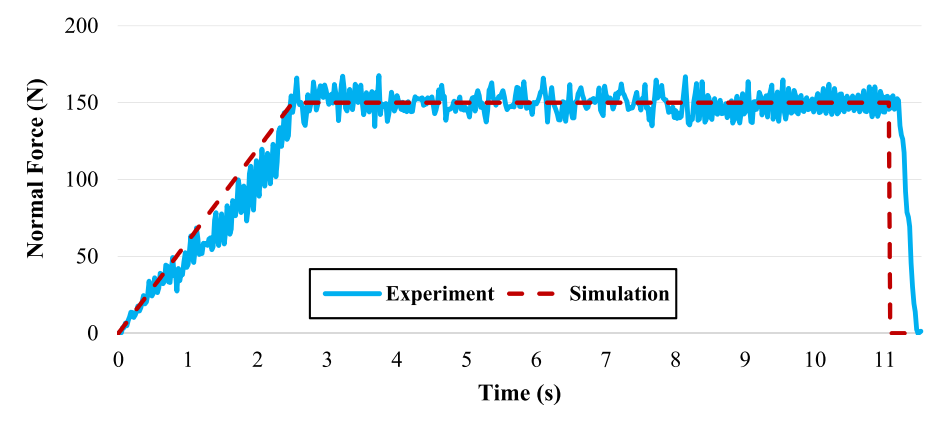


Fig. 4. Comparison of normal force in experiment and FEM.

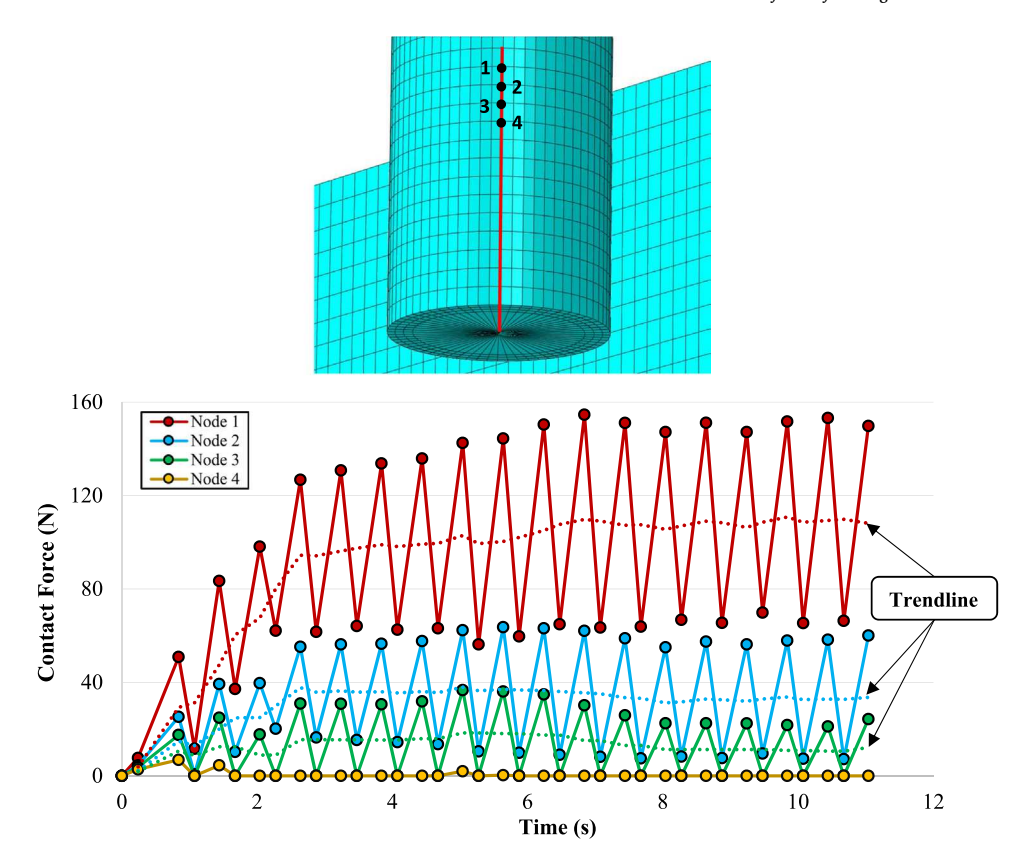


Fig. 6. Normal contact force of Unique Nodal applied on the radial surface of the consumable rod.

substrate tolerate higher forces, while the contact force decreases as the distance of the node from the tip of the consumable rod decreases, and finally, it reaches zero for many of the nodes at the end of the consumable rod and lasts until the end of the deposition phase. In the experiments, the material in contact near the top of the substrate supporting the force was removed during an adequate dwell-phase period until the radial surface of the rod conformed to the substrate and enabled a uniformly distributed contact force across the interface. Thus, the contact pressure was consistent at all points in the contact area after the dwell-phase, resulting in a consistent deposit fabricated through the LFS process. This phenomenon was also observed in the simulation but it lasted for the entire processing time since the dwell-phase period was determined to be short (5 s) (due to high computational time) and also the rod element size was still much larger (in the order of one millimeter) than the thickness of the coatings in experiments (in order of 20-100 µm); therefore, the large elements did not reach of damage criterion.

The force exerted on the substrate's surface was spread out among the points of contact at the interface between the rod and the substrate. The moving average of two data points, represented by a dotted line in Fig. 6, has been plotted to demonstrate the trendline of the force applied on each individual node during the process. Each point's average force contributes to the total normal force at the rod/substrate interface required for the deposition process. As previously discussed, an increasing applied force was exerted within the first 2.5 s of the dwell-phase, resulting in a gradual increase in the applied force of each node.

On the other hand, in the experiment, the consumable rod material points in contact with the substrate reached damage criterion quickly and material was transferred as the deposited coating; therefore, other material points closer to the rod tip contacted the substrate and width of the coating increased until all area on the rod at the interface became involved in the deposition, as discussed previously. This phenomenon continued until all the consumable material points located at the interface became engaged in the deposition process and were subjected

to an equal amount of normal force. A consistent coating with a uniform width during the deposition phase was possible with an ample dwell phase [30]. As mentioned above, larger force was calculated near the top of the substrate, thought to be due to elastic response in the rod and substrate. Therefore, a separate experiment was done to illustrate this phenomenon, as shown in Fig. 7, where the consumable rod traversed from right to left as it deposited material onto the substrate. In the LFS process without a dwell phase, an initial increase in the coating width occurred at the onset of the deposition phase. However, the width increment continued until a stable width and consistent deposition was achieved, as presented in Fig. 7.

The frictional heat generated at the interface of the rod and substrate flows along and toward the rod axis through conduction, resulting in a temperature gradient in the consumable rod. In the course of the LFS process, the lateral surface of the rod is in continuous contact with the substrate surface; therefore, the temperature of the elements in the processing zone increases continuously as frictional heat continues to accumulate in the rod. The maximum process temperature on the center and the radial surface of the consumable rod is presented in Fig. 8. The FEM results demonstrated that, at every moment, the temperature on the radial surface of the rod is slightly higher than that at the center of the rod, as heat conduction between nodes takes time. It was also revealed that the maximum process temperature on the radial surface of the rod followed an overall increasing trend with periodic oscillation. The total number of fluctuations was 38.3 per second, which is equal to the number of complete revolutions of the consumable rod in each second. This fluctuation in temperature occurs because every single node heats up at the processing zone and then cools down due to heat dissipation through conduction, convection, and radiation, as the node moves away from the processing zone. The FEM results show that the center and the lateral surface of the rod at the processing zone reached the temperature of 337.7 K and 341.4 K, respectively, after 11 s of the process, including a 5-second dwell phase and a 6-second deposition phase.



Fig. 7. Consumable rod and coating evolution as contact area increased during LFS process without dwell phase.

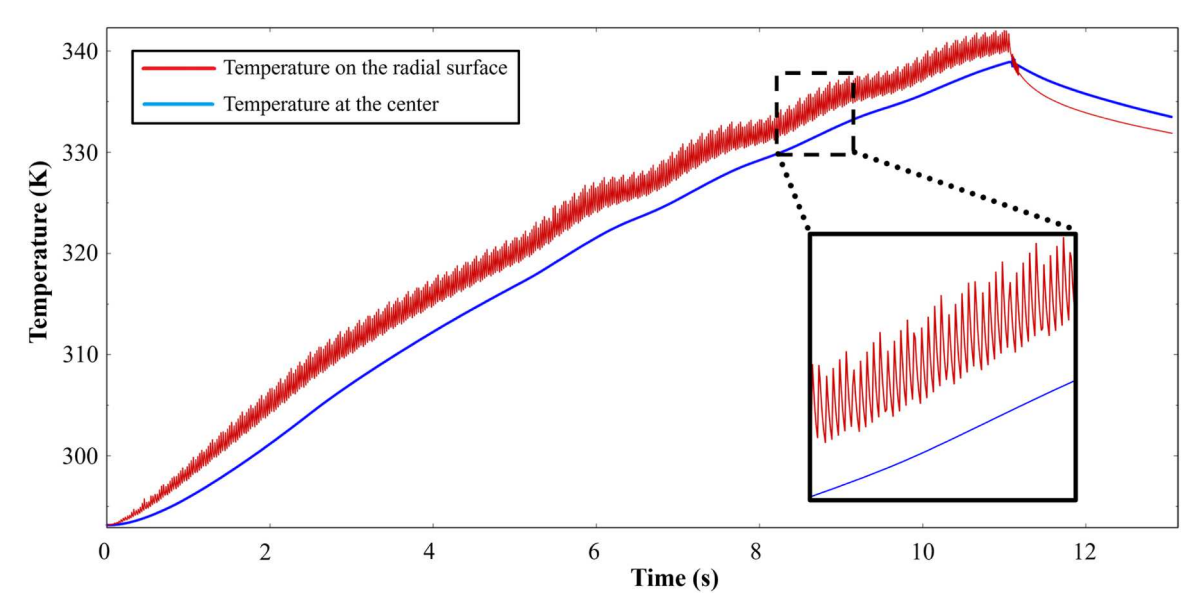


Fig. 8. Temperature recorded on the radial surface and axis of the rod through FEM.

The majority of frictional heat generated at the interface of the rod and substrate was transferred to the aluminum rod due to the higher thermal conductivity of Al6061-T6, which was distributed throughout the rod quickly. On the other hand, a small portion of generated heat

was transferred to the substrate; however, this portion of heat energy was accumulated in the processing zone due to the lower thermal conductivity of the mild steel. This phenomenon resulted in a higher temperature on the steel substrate; therefore, the highest process

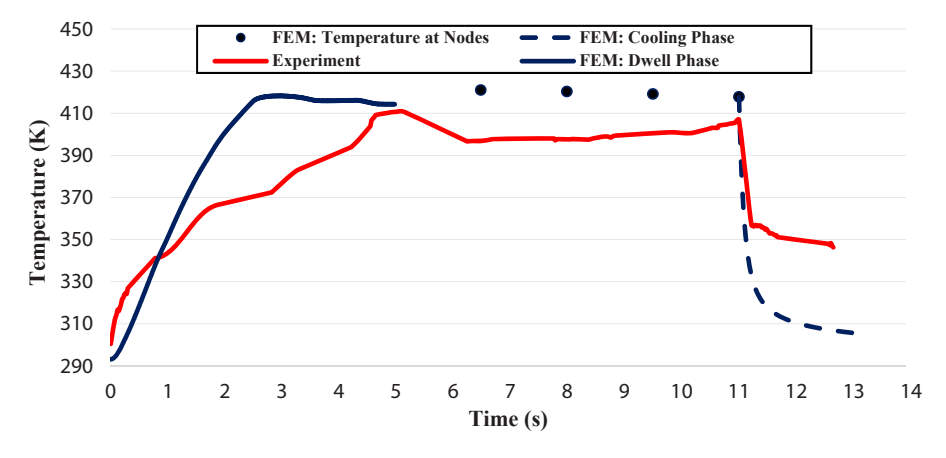


Fig. 9. Maximum process temperature recorded through experiment and finite element modeling.

temperature occurred in the processing zone on the steel substrate.

Fig. 9 presents the evolution of maximum temperature during the experimental analysis and finite element modeling of the LFS process, and the maximum recorded temperature in dwell-phase for these two analyses was 418.3 and 410.7 K, respectively. Although these results are pretty close, the difference between the results of the experiment and FEM is mainly due to the fact that the IR camera could not perfectly see the contact line between the consumable rod and substrate. Another difference between experimental and finite element modeling results is that the maximum temperature in the simulation reaches its maximum value earlier than that in the experimental analysis. This can be explained by the perfect contact at the rod/substrate interface in the simulation, which increases the temperature to its highest value more quickly. In experiments, surface roughness, contact resistance, and imperfect workpiece dimensions lead to incomplete contact at the interface of the rod and substrate, resulting in a slower heat transfer. The rod used in the experiment was not perfectly round and straight, and the substrate surface was not perfectly flat, which resulted in incomplete contact at the rod/substrate interface and a longer time to reach maximum temperature. These results show that the maximum process temperature will finally be defined by the process factors and type of materials employed in the process. The delay in the maximum process temperature of the experiment is concordant with the results presented in [19].

It should be noted that the process temperature can be extracted from the mesh nodes in the FEM. That is why the maximum process temperature obtained from finite element modeling after $t=5\,s$ is presented by few points since the exact temperature at the processing zone is not available when the rod is placed between two nodes. In other words, the temperature of the nodes on both sides of the rod/substrate interface does not represent the actual process temperature, and the actual process temperature only can be obtained when the rod reaches the next node.

The distribution of temperature on the steel substrate is presented in Fig. 10. It was observed that the maximum process temperature occurs in a small zone in the rod/substrate interface. The average temperature of two nodes located in the highest temperature zone represents the simulation result presented in Fig. 9. It was also revealed that the temperature rapidly decreases as the distance from the processing zone slightly increases. The FEM results confirm that the LFS process generates a low and localized processing temperature that minimizes the thermal impact on the material properties.

The localized processing temperature can also be approved by extracting the process temperature profile at the processing zone through the thickness of the substrate. Fig. 11 exhibits the process

temperature at the initial location of the rod/substrate interface over the processing time. It should be noted that the first 5 s of the process take place at that location, after which the processing zone moves gradually. That is why the highest processing temperature (at $D=0\,\text{mm}$) drops rapidly after the dwell phase, while it still increases at a depth of $D=1.75\,\text{mm}$ after $t=5\,\text{s}$, as the heat conduction process needs time. Fig. 11 also revealed a significant difference between the temperature at the substrate surface and a few millimeters in the depth of the plate. A decreasing temperature through depth of the material is desirable, as it can help to minimize thermal stress and distortion inside the material.

The temperature distribution along the axis of the consumable rod and the cross-section of the rod are presented in Fig. 12. It is shown that frictional heat generated at the processing zone heats up the rod surface, and then the rod rapidly cools down as it continues its rotation and leaves the processing zone. This is the reason that causes fluctuation in the elemental node temperature presented in Fig. 8. Even with a high rotational speed of 2300 rpm, the decrease in temperature in a full rotation is noticeable. Comparing the deposition results of AA6061 through LFS in this study and [21] with those obtained through FS in [38] highlights that LFS deposition can be accomplished at significantly lower temperatures compared to FS processes. Also, increasing the length of the rod in contact with the substrate in LFS process does not necessarily cause an increase in the width of the deposit at the beginning of the deposition since the contact force applied by the steel substrate slightly bends the aluminum rod, resulting in a gap between the substrate and the area at the end of the rod. This phenomenon has been experienced several times in experiments and requires an appropriate dwell-phase period for the rod to conform to the substrate and create uniformly distributed contact pressure, and its severity depends on the amount of the normal force and the type of consumable material.

One of the significant advantages of FEM is providing detailed information about stress and strain distribution on the material in a coupled thermo-mechanical process, which is difficult to measure experimentally during the experiment. Fig. 13 shows the distribution of von-Mises stress on the workpiece and the entire rod. Comparing the temperature distribution presented in Fig. 10 and von-Mises stress in Fig. 13 shows that the stress distribution relies on temperature distribution. The temperature gradient generated at the rod/substrate interface created stress all around the processing zone on the substrate. On the other hand, the maximum stress rate on the rod at the processing zone occurred on the radial surface of the consumable rod, and the stress rate decreased near the axis of the rod. The non-uniform stress distribution on the cross-section could be attributed to the vibration of the substrate in contact with the side of the rotating rod.

The spatial velocity at nodes located in the processing zone is

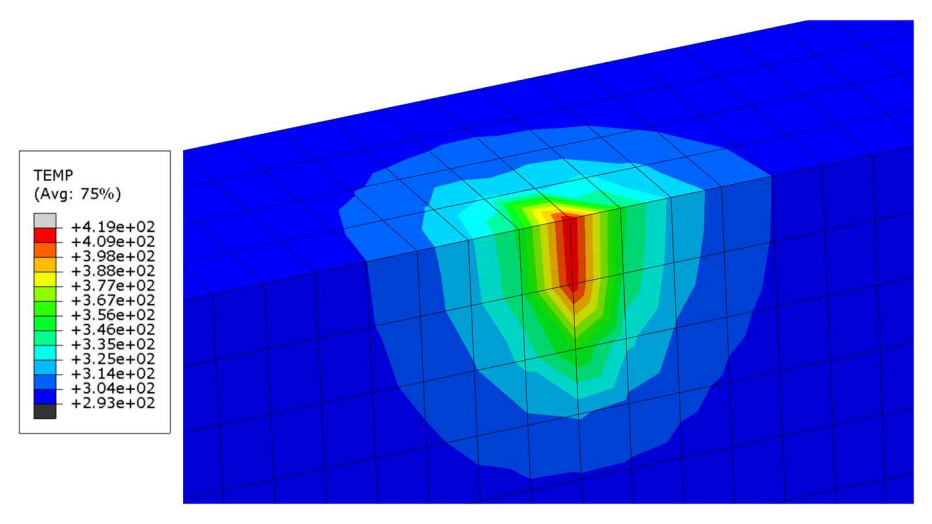


Fig. 10. Temperature distribution on the substrate when the highest substrate temperature obtained.

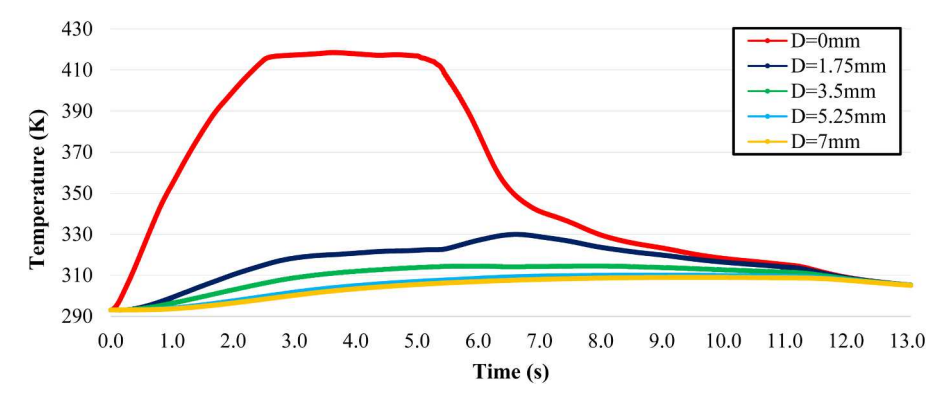


Fig. 11. Process temperature profile through thickness of the substrate at initial contact zone.

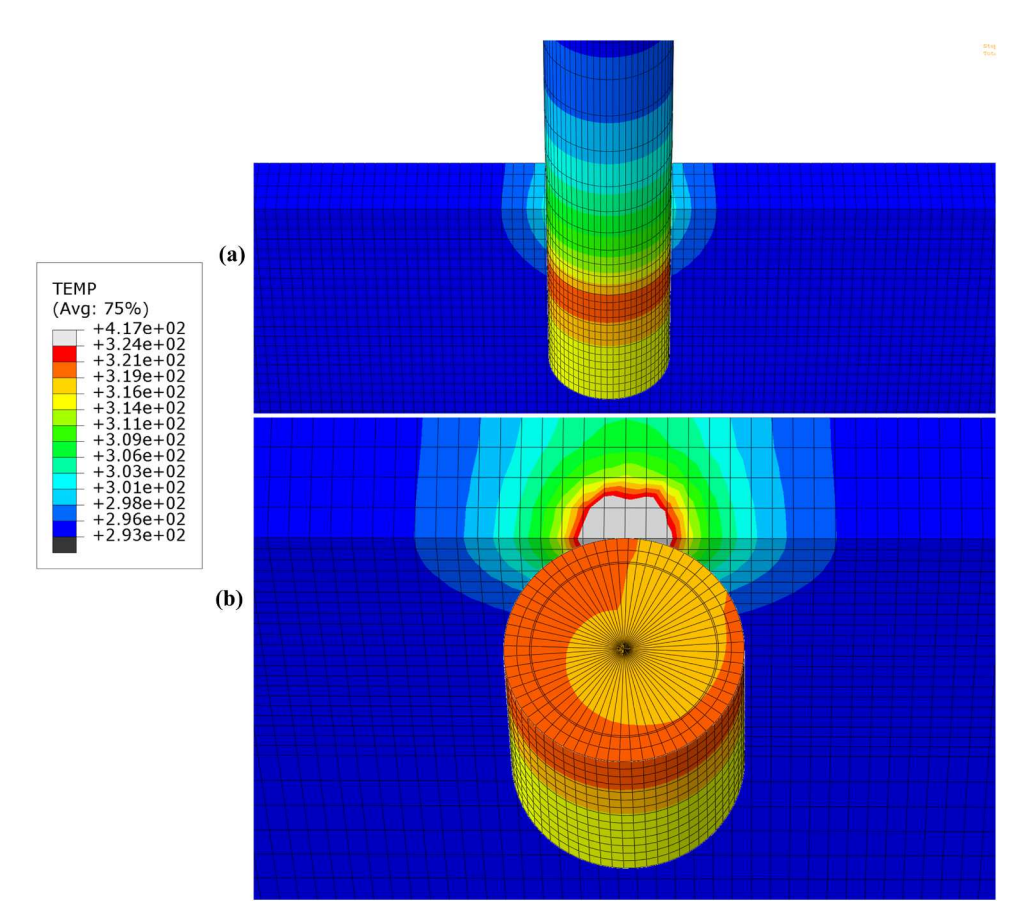


Fig. 12. Temperature distribution along the (a) length of the rod, (b) cross-section of the rod.

presented in Fig. 14. The spatial velocity of three points at the processing zone is presented in Fig. 14 (a), showing a small fluctuation in the velocity. Fig. 14 (b, c) exhibit that the velocity vectors around the consumable rod were not uniform during the surfacing time; since the collision of the rotary rod with the substrate results in high-frequency low-magnitude vibrations, and this phenomenon has been observed in almost all experiments. The generated vibration deforms the uniform velocity vectors around the rod and dislocates the rod from the center of the spatial velocity profile. This shows that contact between the substrate and rotary rod reduces the rotational velocity of the elements in contact with the substrate.

The strain distribution on the substrate and consumable rod is presented in Fig. 15. Based on the strain distribution profile of the substrate, the highest degree of strain occurs at the processing zone on the substrate. Also, the strain profile along the consumable rod shows that the

highest strain level occurs in the area where the rod is confined in the tool holder. This is because the contact force at the interface results in the bending of the rod in that area. The failure of a few aluminum rods during experiments, which was aimed at identifying optimal process parameters for coating fabrication, can be distinctly attributed to the considerable strain observed in this particular zone. The second highest level of strain on the rod occurs in the processing zone. It should be noted that the strain value on the rod at the processing zone is far less compared to the maximum level of strain in the entry of the tool holder.

5. Conclusions

In this investigation, thermo-mechanical finite element analysis was conducted to study the local distribution of variables such as temperatures, local pressure, stress, and strain throughout the consumable rod

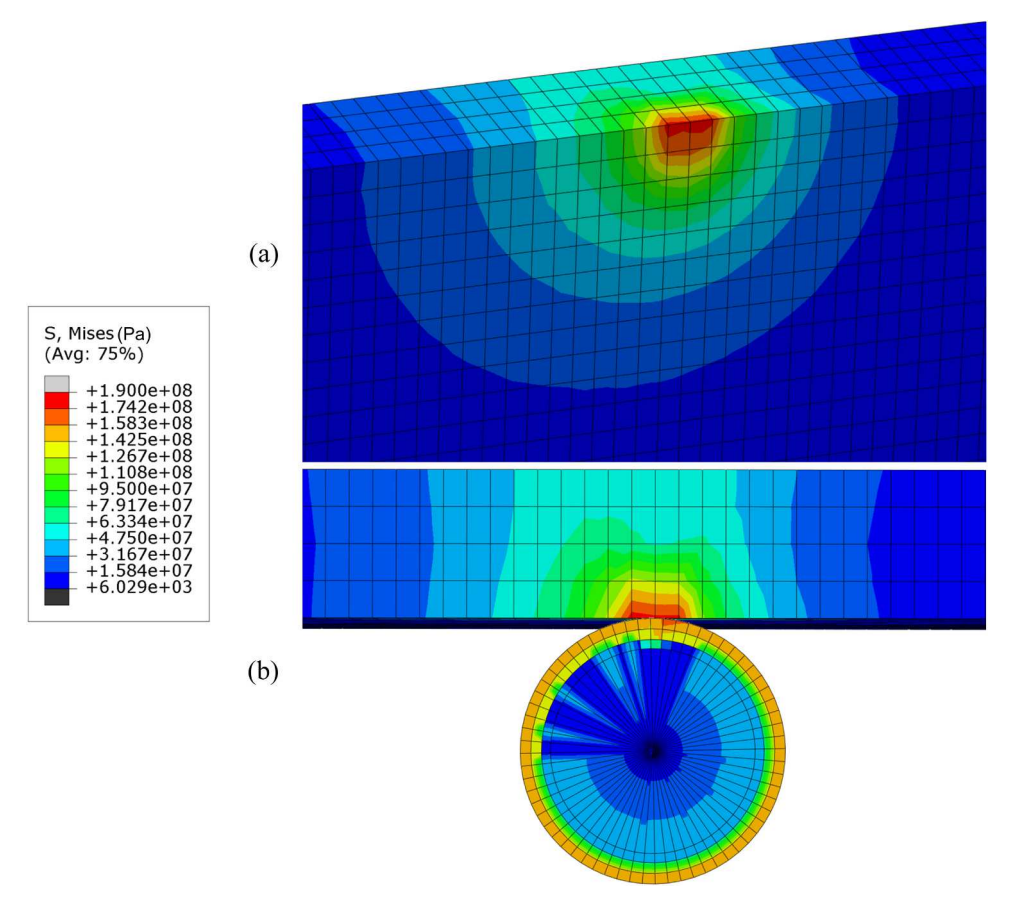


Fig. 13. Stress distribution (a) on the substrate, (b) on the rod.

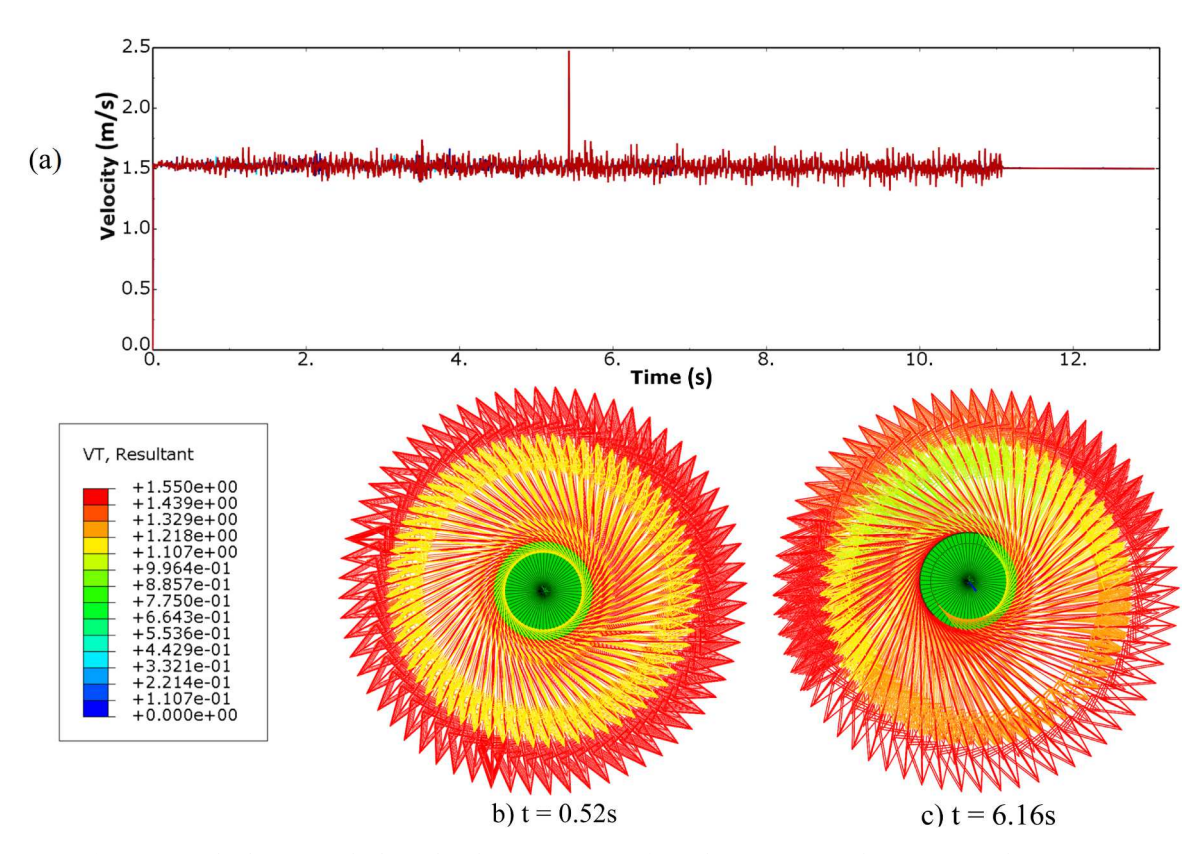


Fig. 14. Special velocity at nodes located in the processing zone for a) the entire process, b) $t=0.52\,s$, and c) $t=6.16\,s$.

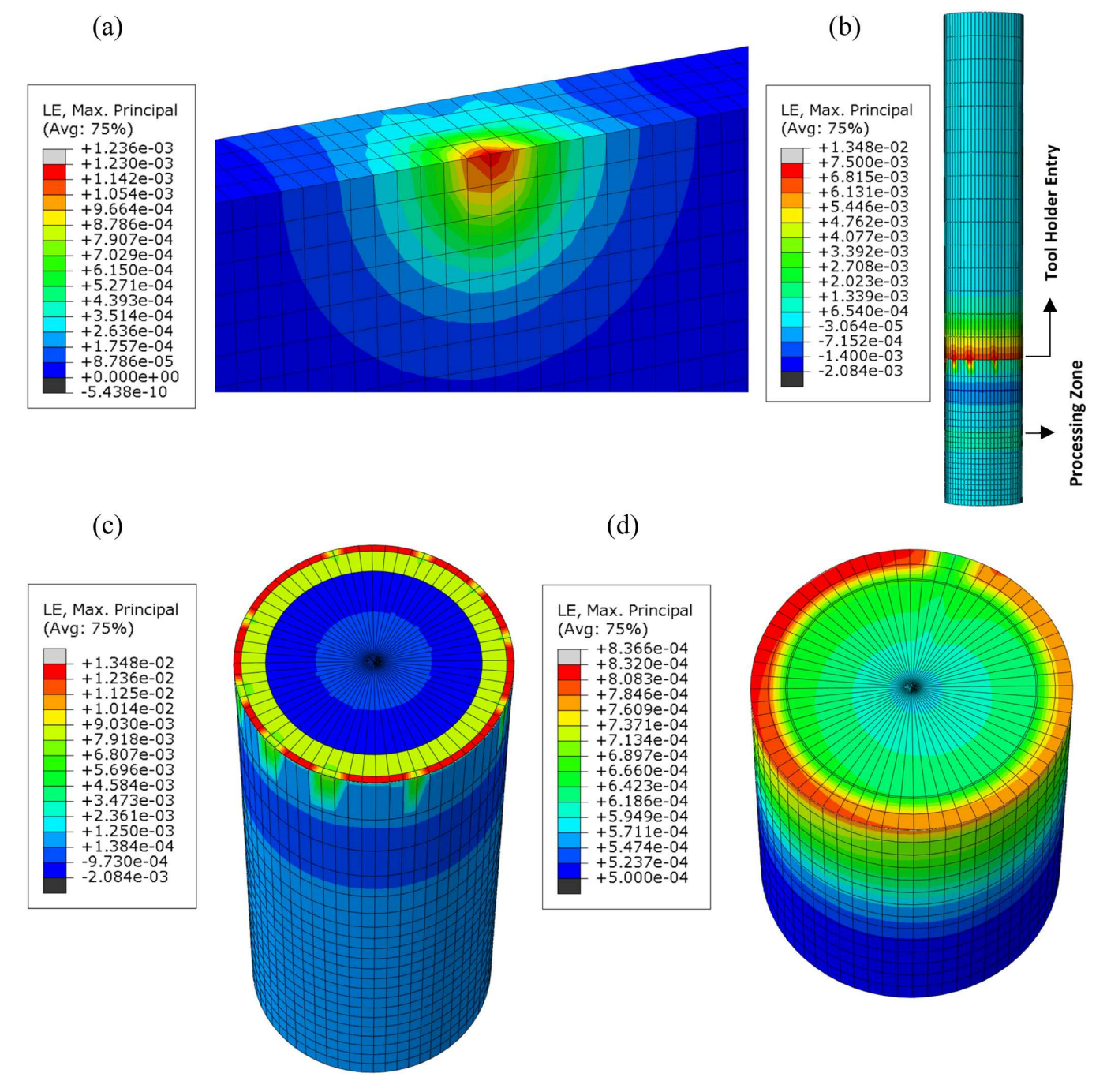


Fig. 15. Strain distribution (a) on the substrate, (b) along the rod, (c, d) on the rod cross-section at t = 5 s (end of the dwell phase).

and workpiece in the LFS process. The results of the FEM were validated through an experimental examination utilizing the same materials and process parameters.

- The FEM confirmed that LFS generates low process temperature localized in a small area, and the temperature rapidly decreased as the distance from the processing zone slightly increased.
- The maximum process temperature on the rod after 11 s (dwell phase and deposition phase) was only 341.4 K, which was much less than that on the substrate recorded during the dwell phase as 418.3 K. This phenomenon was attributed to the difference in thermal conductivity; as heat was rapidly conducted through the rod, but localized in the steel substrate with lower thermal conductivity.
- The results of this investigation revealed that temperature in simulation reaches its maximum value earlier than that in the experimental analysis. This is due to ideal contact at the rod/substrate interface in finite element modeling. In experiments, surface roughness, contact resistance, and imperfect workpiece dimensions lead to incomplete contact at the rod/substrate interface and slower heat transfer.
- Contact force causes deflection in the aluminum rod, resulting in a gap between the substrate and the area at the end of the rod, as captured in the simulation. At the beginning of the experiment, the consumable material points in contact with the substrate reach the damage criterion; therefore, the width of the coating should gradually increase. The results approve the necessity of an appropriate dwell phase period for achieving consistent coating width.

• The highest strain level on the rod occurs at the tool holder entry, where the rod is confined in the tool holder. This is because the contact force at the interface bends the rod in that area. The strain on the rod in the processing zone is far less in comparison. The FEM results highlight the importance of reducing strain and stress levels at the tool holder entry to prevent consumable rod failure. This can be achieved by minimizing the length of the consumable rod outside the tool holder.

CRediT authorship contribution statement

Ebrahim Seidi: Conceptualization, Methodology, Software, Validation, Formal analysis, Investigation, Writing - Original Draft, Visualization, Writing - Review & Editing, **Scott F. Miller:** Conceptualization, Resources, Writing - Review & Editing, Funding acquisition, Supervision.

Declaration of Competing Interest

The authors declare that they have no known competing financial interests or personal relationships that could have appeared to influence the work reported in this paper.

Acknowledgments

This study was supported by National Science Foundation CMMI grant # 1763147, Office of Naval Research award # N000142112861, and General Motors.

References

- [1] Seidi, E., and Miller, S.F., 2019, "Friction Surfacing Using Consumable Tools: A Review," Proceedings of the ASME 2019 14th International Manufacturing Science and Engineering Conference. Volume 2: Processes; Materials, V002T03A048.
- [2] Zhang GF, Jiao WM, Zhang JX. Filling friction stir weld keyhole using pin free tool and T shaped filler bit. Sci Technol Weld Joing 2014;19(2):98–104.
- [3] Huang YX, Han B, Tian Y, Liu HJ, Lv SX, Feng JC, et al. New technique of filling friction stir welding. Sci Technol Weld Join 2011;16(6):497–501.
- [4] Han B, Huang Y, Lv S, Wan L, Feng J, Fu G. AA7075 bit for repairing AA2219 keyhole by filling friction stir welding. Mater Des 2013;51:25–33.
- [5] Rafi HK, Ram GJ, Phanikumar G, Rao KP. "Microstructural evolution during friction surfacing of tool steel H13. Mater Des 2011;32(1):82–7.
- [6] Guo D, Kwok CT, Tam LM, Zhang D, Li X. Hardness, microstructure and texture of friction surfaced 17-4PH precipitation hardening stainless steel coatings with and without subsequent aging. Surf Coat Technol 2020;402:126302.
- [7] Rao KP, Damodaram R, Rafi HK, Ram GJ, Reddy GM, Nagalakshmi R. Friction surfaced Stellite6 coatings. Mater Character 2012;70:111–6.
- [8] Hanke S, Fischer A, dos Santos JF. Sliding wear behaviour of a Cr-base alloy after microstructure alterations induced by friction surfacing. Wear 2015;338:332–8.
- [9] Pereira D, Gandra J, Pamies-Teixeira J, Miranda RM, Vilaça P. Wear behaviour of steel coatings produced by friction surfacing. J Mater Process Technol 2014;214 (12):2858–68.
- [10] Puli R, Ram GJ. Microstructures and properties of friction surfaced coatings in AISI 440C martensitic stainless steel. Surf Coat Technol 2012;207:310–8.
- [11] Nixon RGS, Mohanty BS, Sathish R. Friction surfacing of AISI 316 over mild steel: a characteriation study. Defence Technol 2018;14(4):306–12.
- [12] Rafi HK, Phanikumar G, Rao KP. Corrosion resistance of friction surfaced AISI 304 stainless steel coatings. J Mater Eng Perform 2013;22(2):366–70.
- [13] Tosun G, Ozler L, Ozcan ME. Gradient composite coatings on AA5754 using friction stir process. Surf Eng 2020;36(5):447–55.
- [14] Badheka, K., and Badheka, V.J., 2019, "Wear Behaviour of Boron Carbide Added Friction Surfaced Cladded Layer," Layer. In: Deb D., Balas V., Dey R. (eds)

- Innovations in Infrastructure. Advances in Intelligent Systems and Computing, 757, pp. 395-406.
- [15] Guo D, Kwok CT, Chan SLI. Fabrication of stainless steel 316L/TiB2 composite coating via friction surfacing. Surf Coat Technol 2018;350:936–48.
- [16] Rahmati Z, Aval HJ, Nourouzi S, Jamaati R. Modeling and experimental study of friction surfacing of AA2024 alloy over AA1050 plates. Mater Res Express 2019;6 (8):0865g2.
- [17] Liu X, Yao J, Wang X, Zou Z, Qu S. Finite difference modeling on the temperature field of consumable-rod in friction surfacing. J Mater Process Technol 2009;209(3): 1392–9.
- [18] Pirhayati P, Aval HJ. An investigation on thermo-mechanical and microstructural issues in friction surfacing of Al-Cu aluminum alloys. Mater Res Express 2019;6(5):
- [19] Bararpour SM, Aval HJ, Jamaati R. Modeling and experimental investigation on friction surfacing of aluminum alloys. J Alloys Compd 2019;805:57–68.
- [20] Seidi E, Miller SF. A novel approach to friction surfacing: experimental analysis of deposition from radial surface of a consumable tool. Coatings 2020;10(11):1016.
- [21] Seidi E, Miller SF. Lateral friction surfacing: experimental and metallurgical analysis of different aluminum alloy depositions. J Mater Res Technol 2021;15: 5948–67
- [22] Seidi E, Miller SF. Characterization of Lateral Friction Surfaced AA6063 Coatings. Proc ASME 2021 Int Mech Eng Cong Expos Vol 3: Adanced Mater Des Proc Character Appl 2021.
- [23] Relue W, Seidi E, Hihara LH, Miller SF. Corrosion performance of different aluminum alloy deposits fabricated by lateral friction surfacing. Proc ASME 2021 Int Mech Eng Cong Expos Vol 3: Adanced Mater Des Proc Character Appl 2021.
- [24] Seidi E, Miller SF. Friction surfacing from radial surface of A6063 aluminum alloy consumable tool onto A36 carbon steel. Proce ASME 2020 Int Mech Eng Congr Expos 2020.
- [25] Seidi E, Miller SF. Feasibility of multilayer solid-state deposition via lateral friction surfacing for metal additive manufacturing. J Mater Res Technol 2022;20: 1708–25.
- [26] Seidi E, Miller SF, Carlson BE. Friction surfacing deposition by consumable tools. J Manufact Sci Eng 2021;143(12):120801.
- [27] Bararpour SM, Aval HJ, Jamaati R. An experimental and theoretical investigation of thermo-mechanical issues in friction surfacing of Al–Mg aluminum alloys: material flow and residual stress. Model Simul Mater Sci Eng 2020;28(3):035003.
- [28] Miller, S.F., and Shih, A.J., 2007, "Thermo-Mechanical Finite Element Modeling of the Friction Drilling Process," Journal of Manufacturing Science and Engineering, 2007, 129(3): 531–538.
- [29] Padilla-Llano DA, Schafer BW, Hajjar JF. Cyclic fracture simulation through element deletion in structural steel systems. J Construct Steel Res 2022;189: 107082
- [30] Seidi, E., 2022, "Experimental Analysis and Finite Element Modeling of the Lateral Friction Surfacing Process." Ph.D. Dissertation. University of Hawaii at Manoa.
- [31] Nazemi N, Urbanic J. An experimental and simulation study for powder injection multitrack laser cladding of P420 stainless steel on AISI 1018 steel for selected mechanical properties. J Manufact Sci Eng 2017;140(1):011009. 2018.
- [32] Lazarevic, S., Miller, S.F., Kruger, G., van Niekerk, T., and Carlson, B.E., "Finite Element Analysis of the Friction Stir Forming Process," Proceedings of the ASME 2017 12th International Manufacturing Science and Engineering Conference collocated with the JSME/ASME 2017 6th International Conference on Materials and Processing, Volume 1: Processes, V001T02A006.
- [33] Hajializadeh F, Mashhadi MM. Investigation and numerical analysis of impulsive hydroforming of aluminum 6061-T6 tube. J Manufact Process 2015;20:257–73.
- [34] Umbrello D, M'saoubi R, Outeiro JC. The influence of Johnson-Cook material constants on finite element simulation of machining of AISI 316L steel. Int J Mach Tools Manuf 2007;47:462–70.
- [35] Lesuer, D.R., Kay, G.J., and LeBlanc, M.M., 2001, Modeling Large-Strain, High-Rate Deformation in Metals," Lawrence Livermore National Lab. (LLNL), 15005327.
- [36] Johnson GR, Cook WH. Fracture characteristics of three metals subjected to various strains, strain rates, temperatures and pressures. Eng Fract Mech 1985;21(1): 31–48
- [37] Akbari M, Buhl S, Leinenbach C, Wegener, K. A new value for Johnson Cook damage limit criterion in machining with large negative rake angle as basis for understanding of grinding. J Mater Process Technol 2016;234:58–71.
- [38] Chaudhary B, Jain NK, Murugesan J, Sathiaraj D. Study of microstructure evolution and mechanical properties in friction stir based additive multi-layer manufacturing of Al 6061 alloy: effect of feedstock material form and heat treatment. Mater Today Commun 2023;34:105156.